

Theoretical Analysis and Experimental Research of Surface Texture Hydrodynamic Lubrication

Dan Li

university of Jinan

Xuefeng YANG (✉ me_yangxf@ujn.edu.cn)

College of Mechanical Engineering, University of Jinan, Jinan 250022, China

Wu Yuanbo

university of Jinan

Cheng Jian

hubei university of technology

Wang Shouren

university of jinan

Wan Zhuang

university of jinan

Liu Wenbo

university of jinan

Xia Guofeng

university of jinan

Original Article

Keywords: Hydrodynamic lubrication, Tribological characteristics, Surface texture

Posted Date: September 22nd, 2020

DOI: <https://doi.org/10.21203/rs.3.rs-78890/v1>

License:  This work is licensed under a Creative Commons Attribution 4.0 International License.

[Read Full License](#)

Version of Record: A version of this preprint was published at Chinese Journal of Mechanical Engineering on April 5th, 2022. See the published version at <https://doi.org/10.1186/s10033-022-00691-7>.

Theoretical Analysis and Experimental Research of Surface Texture Hydrodynamic Lubrication

Li Dan^a, Yang Xuefeng^{a,*}, Wu Yuanbo^a, Cheng Jian^b, Wang Shouren^a, Wan Zhuang^a,

Liu Wenbo^a, Xia Guofeng^a

^aCollege of Mechanical Engineering, University of Jinan, Jinan 250022, China

^bCollege of Mechanical Engineering, Hubei University of Technology, Hubei 430068, China

Abstract: This paper established a mathematical model of hydrodynamic lubrication through theoretical analysis, solved the key variables of the mathematical model through simulation and validated the mathematical model using the experimental results. The purpose is to summarize a set of surface texture theory and optimal selection equations for complex working conditions. After comparing the experimental results with the results obtained by the mathematical model, it is found that the two are basically the same in the ranking of the anti-friction properties of different textures, and there is an error of 10%-40% in the friction coefficient value.

Keywords: Hydrodynamic lubrication; Tribological characteristics; Surface texture

1. Introduction

As an effective means of reducing friction, texture has a very broad industrial application prospect. The working mechanism of texture [1] is the theoretical basis of its optimal design. Many studies usually comprehensively analyze the tribological theory and test results, and continuously improve the design of the texture [2-5] to make it more adaptable.

Ryk et al. [6] found that the friction force of the laser-processed surface textured cylinder liner piston ring was reduced by 25%. This is because the surface texture enhances the

1 hydrodynamic lubrication effect under high-speed reciprocating motion. Etsion I et al. [7]
2 constructed a mathematical model for the performance analysis of laser-machined
3 microtextures on the surface of mechanical seals, using liquid film pressure as the main
4 design parameter. The results show that the ratio of hole depth to hole diameter has a very
5 significant effect on pressure. And there is an optimal parameter value that increases friction
6 performance. Wakuda Manabu et al. [8] found that there is a certain size and area ratio to
7 optimize the friction characteristics of the friction pair, while the shape parameters of the
8 texture have little effect on the friction performance. Tonder.K [9] believes that the surface
9 texture can store lubricant in the inlet area. Therefore, the rigidity and damping of the
10 lubricating oil film can be improved, thereby improving the stability of the oil film. Fowell M
11 et al. [10] proposed a new fluid dynamic pressure lubrication mechanism. The pressure
12 difference between the entrance of the texture and the inside of the texture is used to "suck"
13 the lubricating oil into the inside of the texture to form an additional hydrodynamic pressure.
14 This mechanism is considered to be the reason for promoting lubricant film formation and
15 reducing friction and wear on the surface. Hoppermann et al. [11] found that texturing on both
16 friction surfaces would increase friction. Only a texturing process on one surface will reduce
17 friction.

18 Krupka.I et al. [12,13] explored the effect of micro-pit morphology on the thickness of
19 the oil film. The experiment used colorimetric interference method to observe the change of
20 lubricating film thickness. The study found that the micro-pit shape can increase the local
21 minimum oil film thickness. Rahmani et al. [14] used an optimization program to find the best
22 dimensional parameters to increase the pressure-bearing capacity and lubricant flow ratio of
23 the asymmetrically textured slider bearing and reduce the friction coefficient. Charitopoulos

1 et al. [15] found that textures of different shapes and sizes show different improvements on
2 the friction resistance of friction surfaces. Andersson et al. [16] found that the texture with
3 low density and large depth-to-diameter ratio combined with high viscosity lubricating oil can
4 increase the anti-friction properties. Kligerman et al. [17] studied the hydrodynamic effects of
5 laser surface texture in sealed micropores through a finite element model. Compared with the
6 smooth surface, the surface texture can effectively reduce the friction torque and improve the
7 tribological performance of the air seal. Suh et al. [18] used a dynamic model to study the
8 effect of surface texture of the slider air bearing on adhesion and friction. The simulation
9 results show that the surface texture reduces the adhesion and friction by reducing the
10 effective contact area between the slider and the medium surface and preferentially
11 roughening the interface.

12 Lubricating conditions can affect the anti-friction mechanism of texture [19-21]. The
13 friction wear test results alone cannot explain the working mechanism of the surface texture
14 under a certain lubrication condition. The lubrication state of the contact surface is closely
15 related to the oil parameters [22-25]. Thickness of oil film and surface roughness can be used
16 to determine the lubrication state under different operating conditions. The influence of
17 surface texture on the thickness of lubricating oil film should be studied emphatically.

18 In this paper, a set of optimal selection equations for surface texture under different
19 working conditions were summarized. By studying the surface texture and tribological
20 characteristics of different morphology and size features, according to the working conditions
21 of the moving friction pair, the optimal surface texture can be solved and manufactured.

22 **2. Establishment of mathematical model**

23 In this paper, based on the Navier-Stokes equation (N-S equation), a mathematical model

1 of hydrodynamic lubrication of different surface textures was established, and the solution
 2 method of the optimal surface texture model was determined. The purpose is to study how to
 3 choose the optimal solution for different surface textures under different working conditions,
 4 and to provide theoretical guidance for subsequent research.

5 **2.1 Introduction to basic theory**

6 **2.1.1 Derivation of N-S equation**

7 The N-S equation is obtained by substituting and sorting the components of the viscous
 8 fluid motion momentum equation in the form of stress with the expression given by the
 9 generalized Newton's internal friction law [26]. If the fluid is incompressible, the dynamic
 10 viscosity μ is constant. The N-S equation can be simplified as:

$$\begin{aligned}
 11 \quad \rho \frac{dv_x}{dt} &= \rho f_x - \frac{\partial p}{\partial x} + 2\mu \frac{\partial^2 v_x}{\partial x^2} + \mu \frac{\partial}{\partial y} \left(\frac{\partial v_x}{\partial x} + \frac{\partial v_x}{\partial y} \right) + \mu \frac{\partial}{\partial z} \left(\frac{\partial v_x}{\partial z} + \frac{\partial v_z}{\partial x} \right) \\
 12 \quad &= \rho f_x - \frac{\partial p}{\partial x} + \mu \nabla^2 v_x
 \end{aligned}$$

$$13 \quad \text{In the formula, } \nabla^2 = \frac{\partial^2}{\partial x^2} + \frac{\partial^2}{\partial y^2} + \frac{\partial^2}{\partial z^2} \quad (1)$$

14 Similarly, equations in the form of projections on the y and z axes can be derived. The
 15 two ends of the equation are divided by the density at the same time, and the three projection
 16 forms of the N-S equation of incompressible viscous flow can be obtained from the
 17 relationship of dynamic viscosity μ , kinematic viscosity ν and density ρ .

$$\begin{aligned}
 \frac{dv_x}{dt} &= f_x - \frac{1}{\rho} \frac{\partial p}{\partial x} + \nu \nabla^2 v_x \\
 18 \quad \frac{dv_y}{dt} &= f_y - \frac{1}{\rho} \frac{\partial p}{\partial y} + \nu \nabla^2 v_y \\
 \frac{dv_z}{dt} &= f_z - \frac{1}{\rho} \frac{\partial p}{\partial z} + \nu \nabla^2 v_z
 \end{aligned} \quad (2)$$

19 **2.1.2 Couette flow**

1 The N-S equation of viscous fluid motion is a second-order nonlinear partial differential
2 equation, which is difficult to solve. In addition, in practical engineering, the viscous flow
3 with complex flow boundaries is encountered, and with the change of time and space, the
4 flow parameters in the flow field are also constantly affected and changed. But when the flow
5 boundary is relatively simple and the flow parameters are mostly constant, the solution of the
6 flow can be obtained. As a kind of viscous flow, Couette flow is of great significance in
7 engineering, and accurate analytical solutions can be obtained under some conditions [27].

8 The typical form of Couette flow is two infinite planes with a distance of h_0 , in which an
9 incompressible fluid with a dynamic viscosity of μ flows in a fixed direction. Couette flow
10 also includes two other forms. The first is that there is a speed difference between the two
11 planes, so that the two planes produce relative motion but the pressure in the direction of flow
12 does not change. The second is that there is not only a speed difference between the two
13 planes, but also a pressure gradient in the flow direction. At this time, the solution of the
14 linear equation is additive, and the independent solutions of velocity and pressure can be
15 added.

16 **2.2 Basic derivation of theory**

17 Each surface texture corresponds to one or more pressure values and velocity values that
18 can give full play to its tribological properties. This matching mechanism is the core of theory.

19 Before deriving the basic theory, the applicable premise must be determined first:

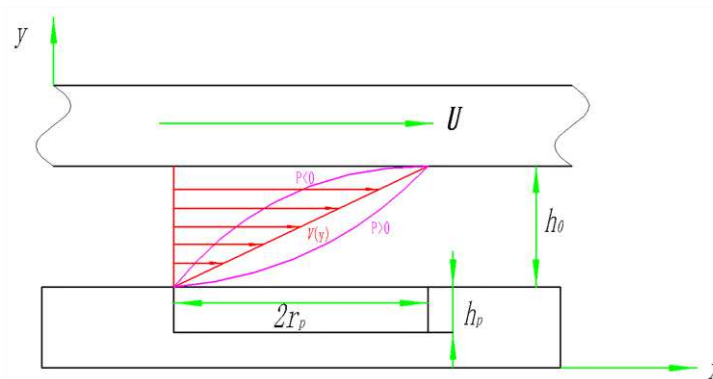
- 20 (1) The effects of volume force such as gravity and magnetic force are ignored.
- 21 (2) Assume that there is no relative sliding between the fluid and solid interface.
- 22 (3) The fluid belongs to a kind of Couette flow, but it is not exactly the same.
- 23 (4) The fluid is Newtonian fluid, and the flow mode is turbulent flow. There may be

1 vortex and turbulent flow in the oil film.

2 (5) Compared with the viscous force of lubricating oil, the inertial force is smaller, so its
3 effect is ignored, including the inertial force when the fluid accelerates and the centrifugal
4 force when the fluid moves in a circular motion.

5 2.2.1 Setting of fluid boundary conditions based on Couette flow

6 As shown in Figure 1, the thickness of the oil film between the two moving friction pairs
7 is h_0 . The lubricating oil is an incompressible fluid with a dynamic viscosity of μ , which is
8 driven by the upper plate to flow positively towards the X axis, and the moving speed of the
9 upper plate is U . The depth of texture is h_p , and the cross-sectional width is $2r_p$. The upper
10 plate moves to the right at speed U , while the lubricating oil has a pressure gradient in the x
11 direction. The red line represents the speed gradient change. The purple line represents the
12 velocity distribution under different pressures. When $P > 0$, the velocity distribution is the
13 rightmost purple line, the pressure promotes the flow of lubricating oil, and the average
14 velocity is greater than the velocity without pressure difference. When $P < 0$, the velocity
15 distribution is the leftmost purple line. At this time, the flow caused by the upper plate is not
16 enough to overcome the flow caused by the reverse pressure difference, so reverse flow
17 occurs.



18 Figure 1. Couette flow

1 The N-S equation can be reduced to:

$$2 \quad v_x(y) = U \frac{y}{h_0} - \frac{1}{2\mu} \frac{dp}{dx} y(h_0 - y) \quad (3)$$

3 By dividing both sides of Equation 3 by y , the equation becomes:

$$4 \quad \frac{v_x(y)}{y} = U \frac{1}{h_0} - \frac{1}{2\mu} \frac{dp}{dx} (h_0 - y) \quad (4)$$

5 Equation 4 is the relationship between the fluid velocity and pressure in the Couette flow
6 form. This equation is a simplified N-S equation based on Couette flow.

7 **2.2.2 Summary of theory formula**

8 Substituting Equation 4 into the pressure-friction conversion equation (Equation 5),
9 Equation 6 is obtained.

$$10 \quad f = \frac{\frac{dp}{dx} \cdot (D_1 + D_2) (D_1^2 - D_2^2) \pi}{n} = \frac{dp}{dx} (D_1 - D_2) \pi \quad (5)$$

$$11 \quad f = \frac{U}{h_0} \frac{y}{(h_0 - y)} \cdot \frac{2\mu}{n} \cdot (D_1 - D_2) \pi \quad (6)$$

12 The conversion equation 5 is derived from the actual experimental conditions in this
13 paper. $dp/dx \cdot (D_1 - D_2)/n$ is the pressure value in the unit area, n is the number of texture
14 distribution on the surface of the test piece, D_1 is the inner diameter of the grinding piece, D_2
15 is the outer diameter of the grinding piece. Equation 5 can be used to combine the
16 hydrodynamic equations with the surface texture parameters, and fully fit the actual working
17 conditions of this article, which improves the accuracy and credibility of the equation.
18 However, there is a certain error in the solution of the pressure in the cell texture area, and this
19 equation also has a certain error. Equation 6 is the relationship between friction force and
20 fluid flow characteristics, it is necessary to continue to derive the equation. The final equation

1 7 is obtained.

$$2 \quad \frac{F}{f} = \frac{P \cdot S}{f} = \frac{P \cdot S (h_0 - y) \cdot n}{\left(\frac{U}{h_0} - \frac{v_x(y)}{y}\right) \cdot 2\mu(D_1 - D_2)\pi} \quad (7)$$

3 2.3 Simplification of theory formula

4 According to the experimental conditions in this paper, the substitution amount is
5 simplified. The outer diameter, inner diameter and contact area of the grinding piece are fixed.
6 The lubricating oil is selected from Mobil Series No. 1 lubricating oil, and the parameters are
7 fixed. In Equation 7, the value of h_0 is critical. Since there is an independent variable y in the
8 film thickness direction, if h_0 is retained, it will increase the difficulty of solving and make the
9 equation have multiple solutions. The value of h_0 is set to 1, and the range of the independent
10 variable y is $[0,1]$, and Equation 8 is obtained.

$$11 \quad u = \frac{P \cdot 0.0000885 \cdot (1 - y) \cdot 24}{\left(\frac{U}{1} - \frac{v_x(y)}{y}\right) \cdot 2 \cdot 0.055 \cdot (0.01 + 0.014)\pi} = \frac{P \cdot (1 - y) \cdot 0.002124}{0.0083 \cdot \left(\frac{U}{1} - \frac{v_x(y)}{y}\right)} \quad (8)$$

12 In Equation 8, the pressure P and speed U need to be set according to the actual working
13 conditions. $\frac{v_x(y)}{y}$ is the first-order partial derivative of the flow speed of the lubricating oil in
14 the X-axis direction. In this model, the velocity v at any point has only the x-axis component,
15 $v_y=v_z=0$, so it can be considered that $v_x=v$. This part needs to obtain data through simulation to
16 solve, the solution process is explained in detail in the simulation analysis section.

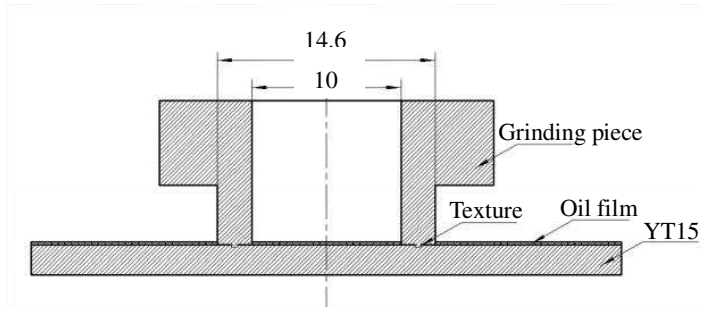
17 3. Simulation analysis

18 The FLUENT module in ANSYS software was used to simulate the hydrodynamic
19 lubrication effect. The purpose is to obtain data that cannot be obtained under experimental
20 conditions to provide data support for the model solution.

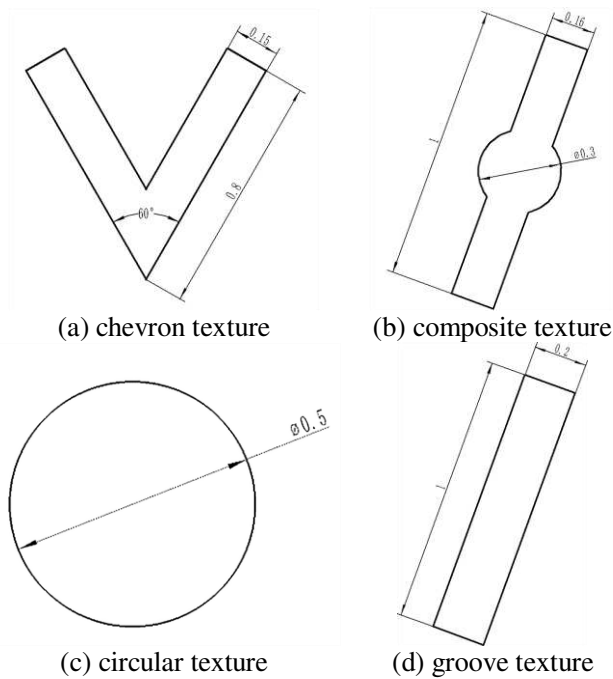
21 3.1 The process of simulation analysis

22 In this paper, four kinds of surface textures are selected as the research object, including

1 groove texture, composite texture, chevron texture and circular texture. The groove texture
 2 and the circular texture are typical textures. As new types of texture, chevron texture and
 3 composite texture have great research value. The upper sample is 45 steel with an inner
 4 diameter of 10 mm and an outer diameter of 14.6 mm, and the lower sample is a round YT15
 5 cemented carbide, as shown in Figure 2. The texture size is shown in Figure 3.



6 Figure 2. Schematic diagram of experiment



7 Figure 3. The size of the texture

8 If the thickness of the oil film is too large, it is inconsistent with the reality, and if it is
 9 too small, the hydrodynamic lubrication effect cannot be reflected. The thickness of the oil
 10 film was set to half of the texture depth. The meshing adopted a mixed mesh of unstructured
 11 tetrahedron and hexahedron. Encryption processing was performed at the boundary of the

1 surface and near the texture. ICEM CFD was used for meshing. The fluid in the simulation
 2 model is lubricating oil. Viscosity grade is ISO VG 68, density is 895 kg/m^3 , viscosity is 61.8
 3 $\times 10^{-6} \text{ mm}^2/\text{s}$. The model selected the k-epsilon Model and used Enhanced Wall Treatment.
 4 When setting the input and output boundary conditions of the simulation model, the
 5 individual texture model is different from the annular overall texture model. Taking the
 6 composite texture as an example, when the texture model is alone, the input face was set as a
 7 pressure inlet. The pressure value was calculated according to the loading force values in the
 8 actual experiment-50 N, 100 N, 150 N and 200 N. The pressure value was obtained from
 9 Equation 9:

$$10 \quad P = \frac{F}{S} = \frac{50\text{N}}{0.0000887\text{m}^2} = 562429.7\text{Pa} , \quad (9)$$

11 The input pressure is 562429.7 Pa at a load of 50 N, and was set to 560000 Pa during
 12 simulation. Similarly, the pressure value is 1120000 Pa at a load of 100 N, is 1680000 Pa at a
 13 load of 150 N, and is 2240000 Pa at a load of 200 N. The output surface was set as a pressure
 14 outlet, and the pressure was the same as inlet. The empirical value of the turbulence intensity
 15 was 10%, and the hydraulic diameter was calculated by Equation 10:

$$16 \quad D = \frac{4A}{P} = \frac{4 \cdot 1 \cdot 0.15\text{mm}^2}{2.3\text{mm}} = 0.26\text{mm} \quad (10)$$

17 Where A is the cross-sectional area of the model and P is the cross-sectional circumference of
 18 the model.

19 The upper end face was set as the speed inlet. The speed value was based on the speed
 20 value in the actual experiment-50 r/min, 100 r/min, 120 r/min, 150 r/min, 180 r/min and 200
 21 r/min. It can be calculated by Equation 11:

$$22 \quad v = \frac{r}{T} = \frac{0.006 \cdot 100\text{m/s}}{60} = 0.01\text{m/s} \quad (11)$$

23 When the rotation speed is 100 r/min, the average linear velocity of the grinding piece is 0.01

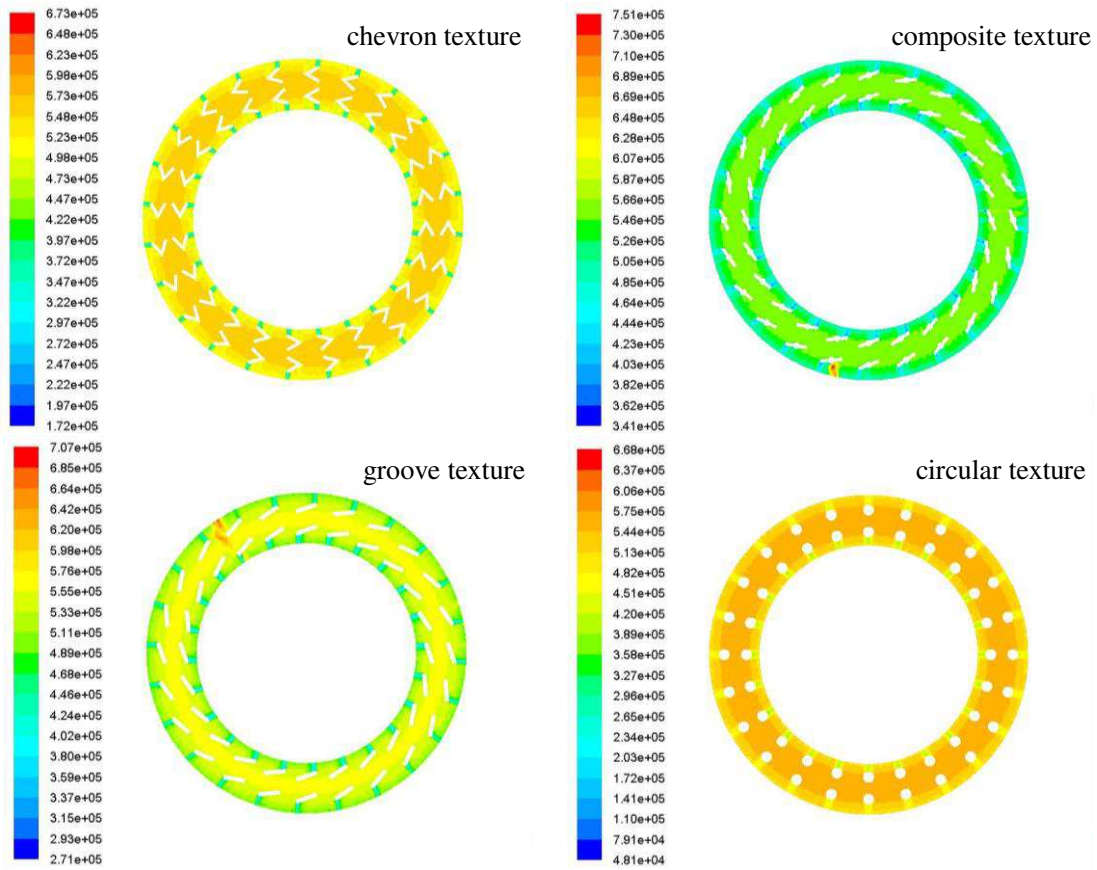
1 m/s. Similarly, when the rotation speeds are 50 r/min, 120 r/min, 150 r/min, 180 r/min and
2 200 r/min, the corresponding linear velocity values of simulation model are 0.05 m/s, 0.12
3 m/s, 0.15 m/s, 0.18 m/s and 0.2 m/s. The algorithm used the SIMPLE method. The
4 momentum equation adopted two-level upwind style discreteness. The remaining energy
5 equations adopted the first-order upwind style discreteness. The relaxation factors remained at
6 their default values. The calculation starting point was the input face.

7 When the texture model is overall texture. The upper end face was set as the pressure
8 input face, and the pressure value was the same as the single texture model. The inner and
9 outer rings of the model were set as pressure output surfaces. In actual experiments, the
10 pressure on both sides is atmospheric pressure. Therefore, the output surface pressure value in
11 the simulation model is zero. The other surface was set as a moving wall and rotates around
12 the center according to the rotation speed. The algorithm, momentum equation, energy
13 equation and relaxation factor were the same as the individual texture model.

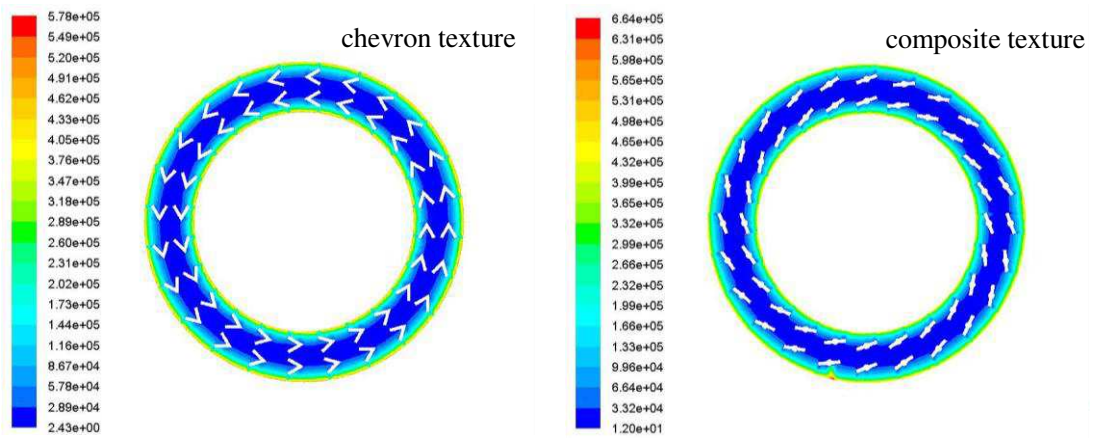
14 **3.2 Simulation results**

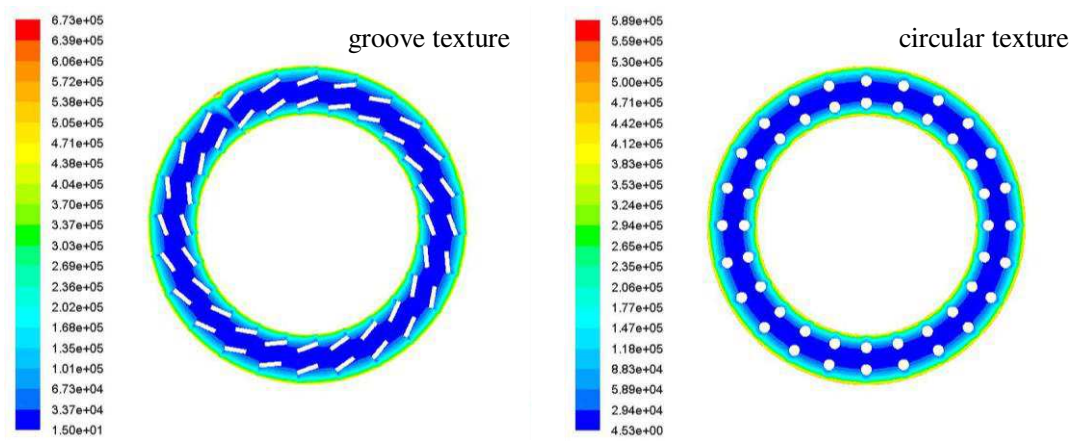
15 Figure 4 shows the total pressure cloud diagram and dynamic pressure cloud diagram of
16 the four textures under the same experimental conditions (50 N, 100 r/min). As shown in
17 Figure 4(a), the high-pressure areas of the four textures are in the middle of the double-row
18 texture. The high-pressure areas of chevron, composite, and circular textures are more
19 concentrated and the boundaries are obvious, while the high-pressure areas of the groove
20 texture have blurred boundaries, and there is no significant difference in pressure values
21 across the texture surface. From the numerical point of view, the pressure value of the circular
22 texture is the largest, the pressure value of the chevron texture is second only to the circular
23 texture, and the pressure value of the groove texture is the smallest. As shown in Figure 4(b),

- 1 the dynamic pressure distribution on the surface of the four textures is basically the same, and
- 2 they are relatively small. This is because the dynamic pressure value at the position close to
- 3 the wall is smaller than the center position of the fluid flow.



4 (a) Overall pressure cloud diagram





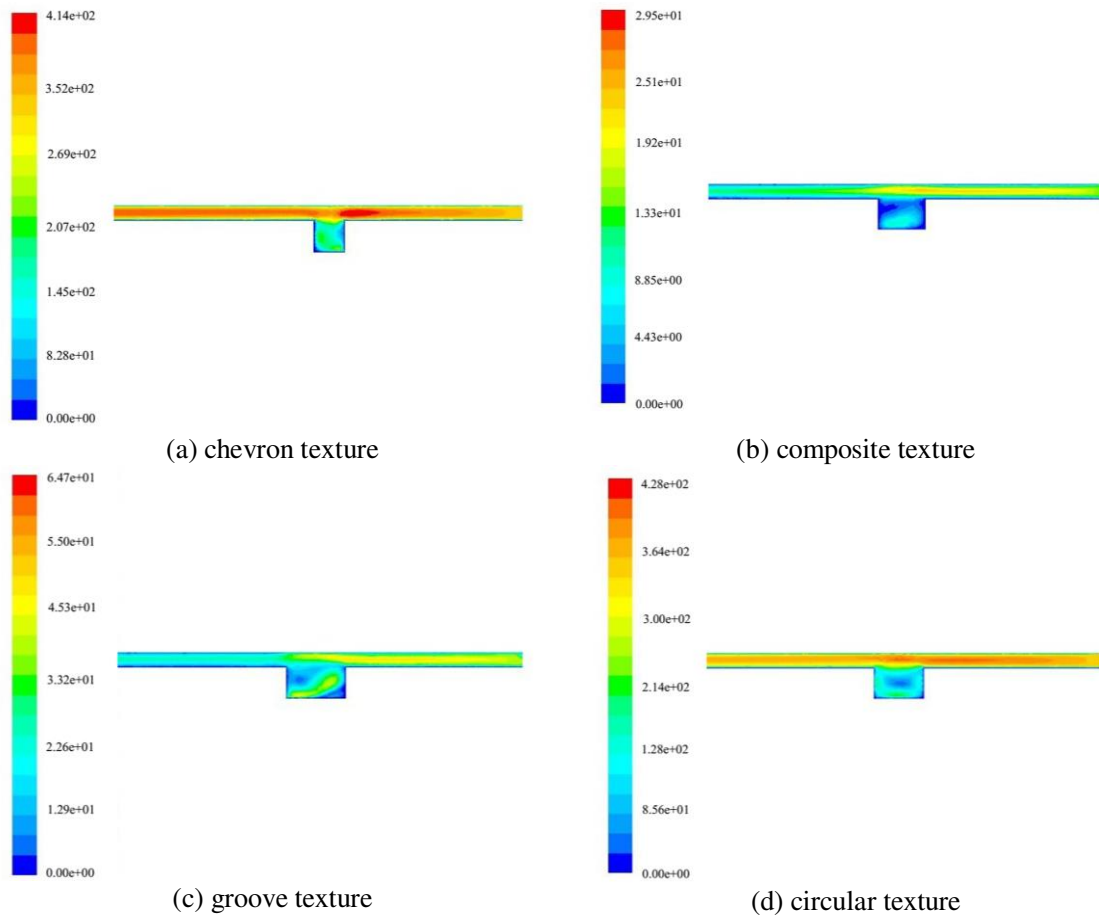
(b) Dynamic pressure cloud diagram

Figure 4. Overall pressure cloud diagram and dynamic pressure cloud diagram of overall texture

3.3 Numericalization of simulation results

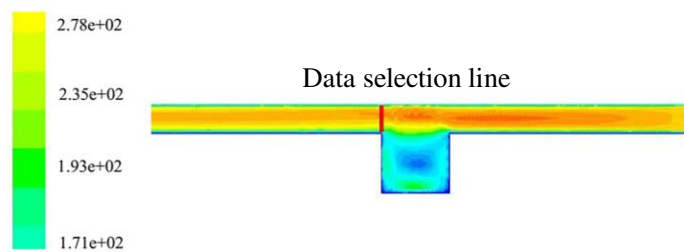
3.3.1 Data collection

When constructing a mathematical model, the partial derivative of velocity v with respect to y is unknown. Because it is not easy to measure in actual experiments, it needs to be calculated according to the simulation analysis results. Using FLUENT software, the velocity clouds of the four textures are obtained when the loading force is 50 N and the rotation speed is 100 r/min. The results are shown in Figure 5. According to the simulation results, a vertical line is taken at the output end face, as shown in Figure 6. FLUENT's data processing function is used to output ASCII code data, and then Notepad ++ is used to import the data into an Excel table after processing. The values in the data include x-coordinate, y-coordinate, z-coordinate, and velocity-magnitude. According to the theoretical analysis part, the value of $v_x(y)$ is velocity-magnitude. And according to Figure 6, the speed value is 100 mm/s -300 mm/s, the actual speed is about 1-10 mm/s, so in order to rigorous and accurate mathematical model, the data needs to be processed. All simulation values were reduced by 100 times.



1

Figure 5. Cloud diagram of velocity distribution



2

Figure 6. Schematic diagram of the location of the data selection line

3 3.3.2 Simulation equations of key variables

4

After obtaining the simulation data value, the function equation is solved according to the numerical value, and the solving process is carried out with the help of MATLAB toolbox.

5

6

The processed data was imported into the MATLAB workspace and named for different data

7

groups. The Curve Fitting toolbox was selected to perform curve fit analysis on the data in the

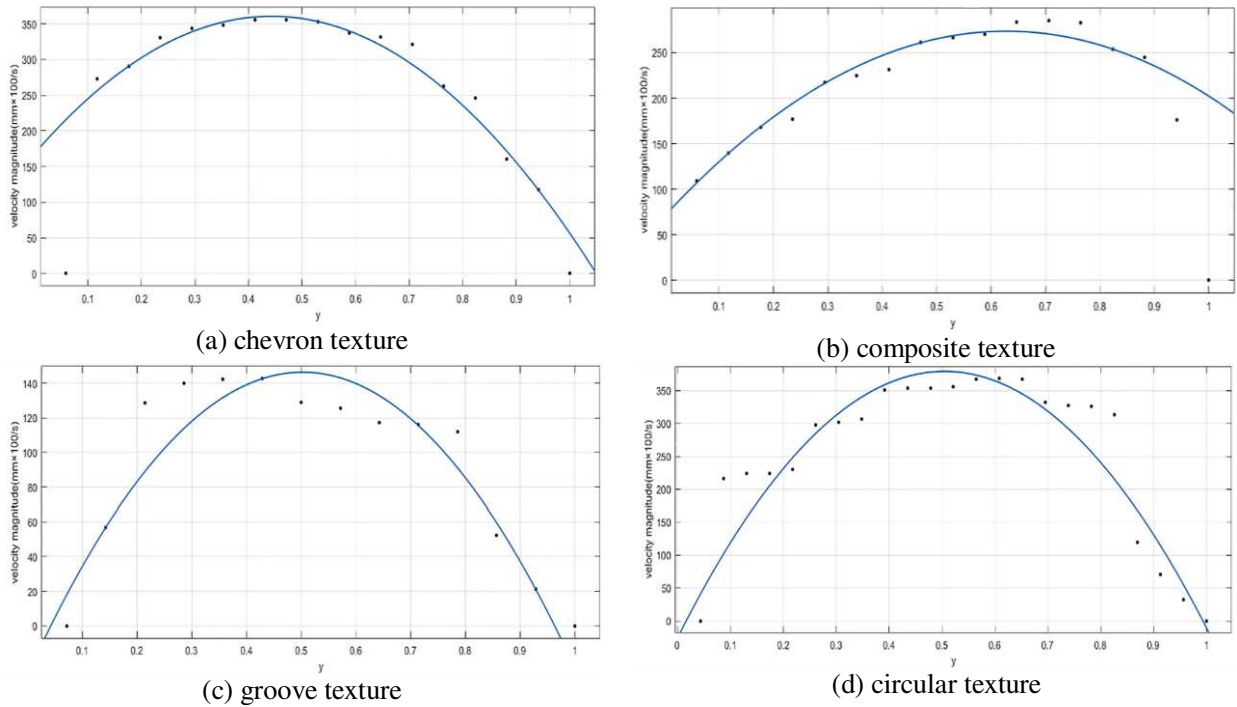
8

work area to obtain a function equation. Figure 7 shows the fitting curves of four textures.

9

The abscissa is the y value, and the y -axis zero position is at the top of the data selection line

1 in Figure 6. The ordinate is the speed value. R-square is the degree of equation fit. To
 2 facilitate the solution of the mathematical model, replace y in the original formula with x . The
 3 four texture fitting equations are shown in Table 1.



4 Figure 7. Fitting curves of four textures

5 Table 1. Simulation equations of four textures

Texture	Chevron texture	Composite texture	Groove texture	Circular texture
Equation	$f(x) = P_1 \cdot x^2 + P_2 \cdot x + P_3$	$f(x) = P_1 \cdot x^2 + P_2 \cdot x + P_3$	$f(x) = P_1 \cdot x^2 + P_2 \cdot x + P_3$	$f(x) = P_1 \cdot x^2 + P_2 \cdot x + P_3$
	P_3	P_3	P_3	P_3
P_1	-9.52	-5.146	-6.904	-15.90
P_2	8.377	6.462	6.942	16.06
P_3	1.791	0.7071	-0.2811	-0.2623
R-square	0.946	0.912	0.8769	0.8741

6 4. Friction and wear experiment

7 4.1 Design of the experiment

8 4.1.1 Design of surface texture

9 The area occupancy rate of the four textures is 10%. The processing parameters of the

1 four textures are shown in Table 2.

2 Table 2. Processing parameters of four textures

Texture	Chevron texture	Composite texture	Groove texture	Circular texture
Distribution form	Double row	Double row	Double row	Double row
Unit number	48	48	48	48
Area of unit texture	0.2 mm ²	0.19 mm ²	0.2 mm ²	0.2 mm ²
Area occupancy rate	10.8%	10%	10.8%	10.8%

3 Before processing the texture on the surface of the workpiece, it is necessary to pre-treat
4 the test piece. Boron carbide powder was used to grind the test piece to smooth on frosted
5 glass. Diamond polishing paste was used to polish the test piece on the polishing machine
6 until the surface was mirror-like. The test piece was placed in an ultrasonic cleaner to clean
7 the surface dirt. The polished samples were measured on a Mitutoyo SJ-410 surface
8 roughness measuring instrument and the average surface roughness of all test pieces was
9 0.045. A Libra-HE femtosecond laser was used to process the surface texture.



10 Figure 8. Friction and wear testing machine, 45 steel, and workpiece after processing texture

11 4.1.2 Experimental scheme

12 The experiment used MMG-10 friction and wear testing machine. The lubricating oil
13 code is 5W-40, and the viscosity at normal temperature is 0.055 Pa •s. The variable selects the

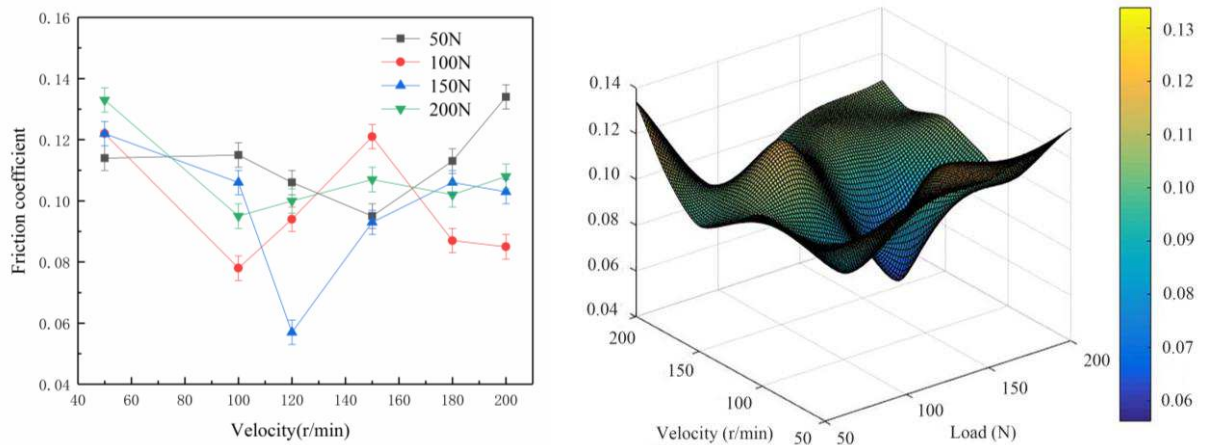
1 loading force and speed, and the parameter values are shown in Table 3. Four variables were
 2 selected for the loading force and six variables for the rotation speed, and a total of 96 groups
 3 of experiments were conducted, each group of experiments for 10 minutes.

4 Table 3. Experimental parameter values

Texture	Loading force (N)	Rotation speed (r/min)	Condition	Contact method
Chevron texture	50	50	25°C Atmospheric pressure Oil lubrication	Face to face
Composite texture	100	100		
Groove texture	150	150		
Circular texture	200	180		
		200		

5 **4.2 Experimental results**

6 **4.2.1 Chevron texture**

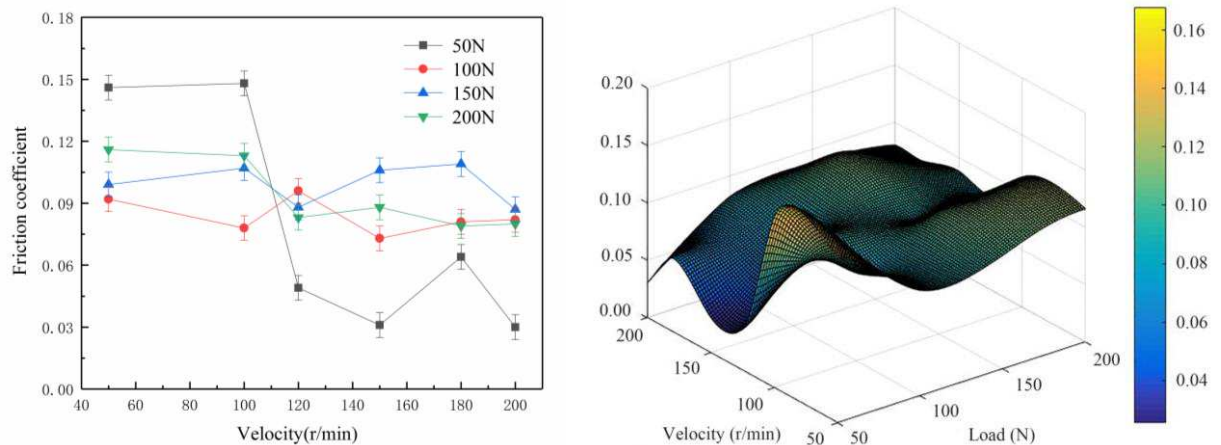


7 Figure 9. Experimental results of chevron texture

8 Figure 9 is the experimental results of chevron texture under different loading force and
 9 speed. According to the three-dimensional graph, the distribution interval of the friction
 10 coefficient of chevron texture is [0.05, 0.14], and the range is 0.09. The lowest point of the
 11 entire curved surface is when the loading force is 150 N and the rotation speed is 120 r/min.
 12 The highest points are at the loading force of 200 N and the speed of 50 r/min and the loading
 13 force of 50 N and the speed of 200 r/min, respectively. The point where the friction coefficient

1 is the smallest is the value when the loading force and the rotation speed are at an
 2 intermediate level. The friction coefficient at a loading force of 50 N and a rotation speed of
 3 50 r/min and a loading force of 200 N and a rotation speed of 200 r/min is close and small.
 4 This shows that there is an optimal matching interval between loading force and speed. When
 5 the difference between loading force and speed is too large, the friction coefficient will
 6 increase. When the speed is constant, the friction coefficient decreases with increasing loading
 7 force. When the loading force is constant, the friction coefficient decreases with increasing
 8 speed. When the loading force is 200 N, the friction coefficient is small and the change is
 9 relatively stable, indicating that the chevron texture shows good hydrodynamic lubrication
 10 characteristics under high load conditions. It proves that the chevron texture has strong
 11 pressure bearing capacity and is suitable for high load conditions.

12 4.2.2 Composite texture



13 Figure 10. Experimental results of composite texture

14 According to the three-dimensional diagram of Figure 10, the distribution interval of the
 15 friction coefficient of the composite texture is [0.03, 0.148], and the range is 0.118. The entire
 16 curved surface presents a two-step shape. The lowest point of the curved surface is when the
 17 loading force is 50 N and the rotation speed is 150 r/min, and the loading force is 50 N and
 18 the rotation speed is 200 r/min. The highest points are when the loading force is 50 N and the

1 rotation speed is 50 r/min, and the loading force is 50 N and the rotation speed is 100 r/min.
2 Both the maximum and minimum friction coefficients are when the loading force is 50 N.
3 When the rotation speed is greater than 100 r/min, the friction coefficient will appear a
4 stepwise decline under each loading force, and then it will tend to be gentle. When the loading
5 force is 50 N, the range of friction coefficient is extremely large, and the fluctuation is severe.
6 At low speeds, the friction coefficient increases with increasing loading force. At high speeds,
7 the friction coefficient decreases with decreasing loading force. This shows that for composite
8 textures, the influence of speed is greater than the loading force. As shown in the line chart,
9 when the rotation speed is constant, the friction coefficient fluctuates with the increase of the
10 loading force. When the loading force is constant, the friction coefficient decreases with
11 increasing speed. When the loading force is 100 N and above, the friction coefficient value is
12 small and tends to be stable. When the loading force is 100 N, the friction coefficient is more
13 stable and smaller than when the loading force is 150 N and 200 N. It shows that the
14 composite texture shows good hydrodynamic lubrication characteristics under high-speed and
15 medium-high load conditions. It is proved that the composite texture contains the
16 characteristics of groove texture and circular texture, and has a certain pressure-bearing
17 capacity and the ability to promote the flow of lubricating oil.

18 **4.2.3 Groove texture**

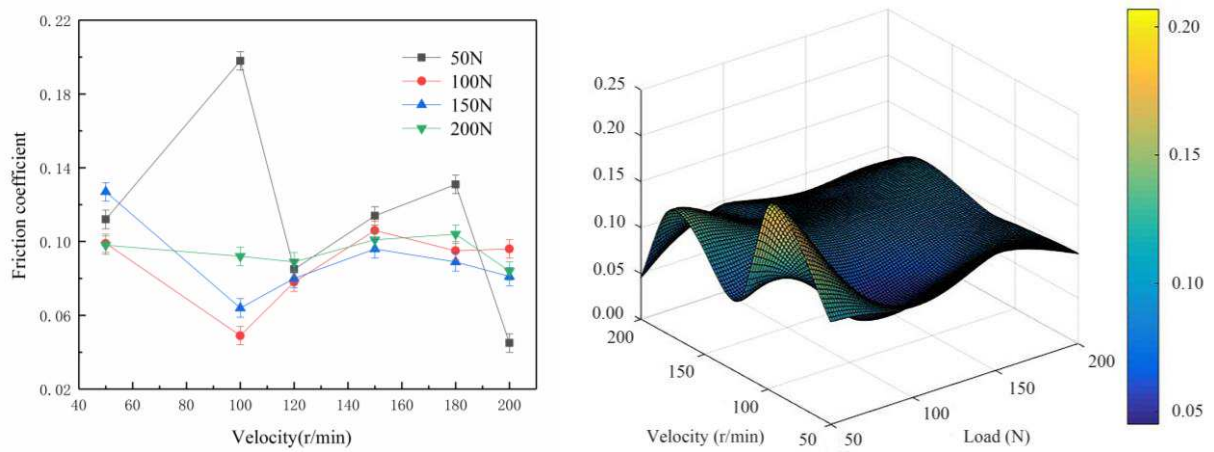
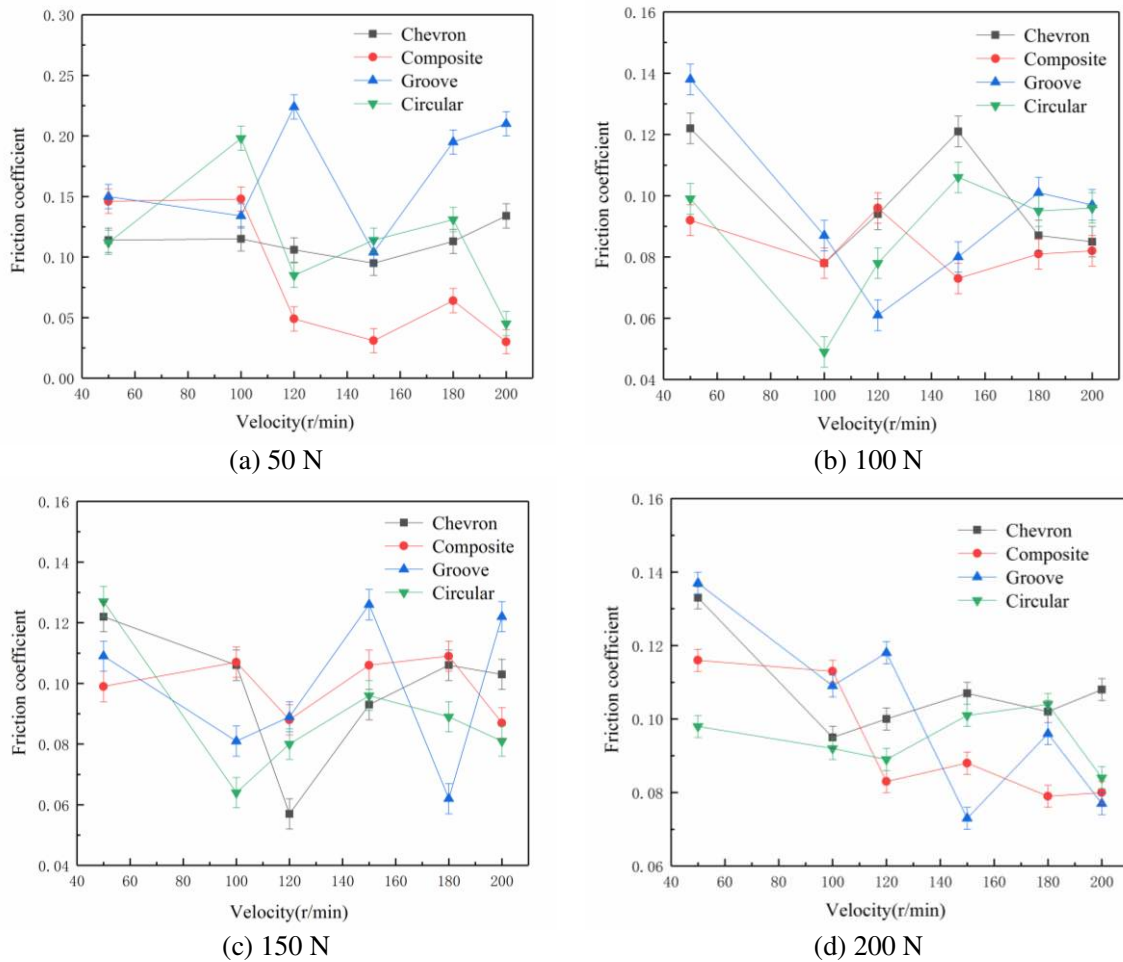


Figure 12. Experimental results of circular texture

According to the three-dimensional diagram of Figure 12, the distribution interval of the circular texture friction coefficient is [0.045, 0.198], and the range is 0.153. The highest point is when the loading force is 50 N and the speed is 100 r/min. The lowest points are when the loading force is 100 N and the rotation speed is 100 r/min, and the loading force is 50 N and the rotation speed is 200 r/min. The friction coefficient fluctuates greatly when the loading force is 50 N, and the curved surface is hump-shaped. The friction coefficient gradually stabilizes with the increase of the loading force, and it shows a plane-like distribution. As shown in the line chart, when the speed is constant, the friction coefficient decreases with the increase of the loading force. When the loading force is 200 N, the friction coefficient is small and the change is relatively stable. When the loading force is constant, the friction coefficient increases with the increase of speed. When the rotation speed is 100 r/min and the loading force is 100 N, 150 N, 200 N, the friction coefficient is the minimum value under the loading force. It shows that the circular texture shows excellent stability under high load and medium speed conditions. It is proved that the circular texture has strong pressure bearing capacity and strong stability, and is suitable for high load conditions.

4.2.5 Friction coefficients of different textures under the same loading force



1 Figure 13. Variation curve of friction coefficient of different textures under the same loading force

2 Figure 13 is the variation curve of friction coefficient of different textures under the
 3 same loading force. When the loading force is 50 N, 100 N and the rotation speed is low, the
 4 friction coefficient of chevron texture and circular texture is the lowest. At high speeds, the
 5 friction reduction effect of the composite texture is most obvious. When the loading force is
 6 150 N, the friction coefficient of chevron, composite and circular texture changes in the same
 7 trend, showing a large undulating wave shape. The rotation speed at the lowest friction
 8 coefficient of the circular texture is 100 r/min, the chevron texture is 120 r/min, and the
 9 groove texture is 180 r/min. The friction coefficient of the composite texture changes steadily
 10 and there are no huge fluctuations. When the loading force is 200 N and the rotation speed is
 11 low, the friction coefficient of chevron texture and circular texture is lower. At high speeds,

1 the friction coefficient of the composite texture and the groove texture is lower. The chevron
2 texture has a strong pressure-bearing ability, but it can only play a good anti-friction effect at
3 low speeds, and the anti-friction effect decreases significantly at high speeds. Due to the weak
4 pressure bearing capacity of the groove texture, the friction coefficient is unstable under high
5 load. However, due to the characteristics of improving fluidity, the friction coefficient is small
6 at high speeds. The composite texture consists of groove and circle. The composite texture
7 still shows good anti-friction effect under high load and high speed working conditions.

8 The above research shows that the chevron texture has a small and stable friction
9 coefficient at high loads. It shows that chevron texture is suitable for high load conditions.
10 The composite texture has a small friction coefficient under high-speed and medium-high
11 load conditions. It shows that the composite texture is suitable for high-speed and
12 medium-high load conditions. The friction coefficient of the groove texture does not decrease
13 significantly when the loading force increases. When the rotation speed is constant, the
14 friction coefficient decreases as the loading force decreases. It shows that the pressure
15 capacity of the groove texture is weak, and it is suitable for medium speed and low load
16 working conditions. The friction coefficient of the circular texture tends to be stable as the
17 loading force increases. When the loading force is constant, the friction coefficient will
18 increase with the increase of speed. It shows that the circular texture has strong pressure
19 bearing capacity and weak flow promotion ability, which is suitable for medium and low
20 speed and high load working conditions.

21 **5. Solution and verification of mathematical model**

22 **5.1 Combination of simulation formula and theoretical formula**

23 **5.1.1 Determination of key parameters**

1 According to the simulation model, the oil flow velocity equations under different
 2 surface texture conditions are obtained, and the first derivative is obtained by combining the
 3 mathematical model with the results. The results are shown in Table 4. After obtaining the key
 4 equation, it is substituted into the theory equation.

5 Table 4. Derivatives of four texture equations

Texture	Chevron texture	Composite texture	Groove texture	Circular texture
Equation	$F'(x) = 2 \cdot K_1 \cdot x + K_2$	$F'(x) = 2 \cdot K_1 \cdot x + K_2$	$F'(x) = 2 \cdot K_1 \cdot x + K_2$	$F'(x) = 2 \cdot K_1 \cdot x + K_2$
K_1	-9.52	-6.904	-6.904	-15.90
K_2	8.377	6.942	6.942	16.06

6 5.1.2 Substitution of key parameters

7 The above key equation is substituted into Equation 8 to obtain Equation 12:

$$8 \quad u = \frac{P \cdot (1-x) \cdot 0.002124}{0.0083 \cdot (U - F'(x))} \quad (12)$$

9 Equation 12 is further simplified to obtain Equation 13:

$$10 \quad u = \frac{0.256 \cdot P(1-x)}{(U - 2 \cdot K_1 \cdot x - K_2)} \quad (13)$$

11 Where K_1 and K_2 are equation parameter values of different surface textures. The
 12 equations of the four surface textures are as follows.

13 The equation of chevron texture is:

$$14 \quad u = \frac{0.256 \cdot P(1-x)}{(U + 19.04 \cdot x - 8.377)} \quad (14)$$

15 The equation of composite texture is:

$$16 \quad u = \frac{0.256 \cdot P(1-x)}{(U + 10.292 \cdot x - 6.462)} \quad (15)$$

1 The equation of groove texture is:

$$2 \quad u = \frac{0.256 \cdot P(1-x)}{(U + 13.808 \cdot x - 6.942)} \quad (16)$$

3 The equation of circular texture is:

$$4 \quad u = \frac{0.256 \cdot P(1-x)}{(U + 31.80 \cdot x - 16.06)} \quad (17)$$

5 **5.2 Verification of formula**

6 According to the above equation, the relationship between the friction coefficient u , the
7 load P , and the rotation speed U can be obtained, and the value range of x is $[0, 1]$. After
8 substituting the loading force and speed under different working conditions into equations 14,
9 15, 16, and 17, the minimum value of the equation in the interval $[0,1]$ is solved, and the
10 function values of the four equations are compared. The texture with a smaller function value
11 is the better texture, which can achieve the purpose of selecting the optimal texture according
12 to different working conditions.

13 In order to verify the accuracy of the formula, an experimental working condition was
14 selected to compare the experimental results with the calculation results of the formula. The
15 loading force of 50 N and the speed of 100 r / min are selected to solve the minimum value of
16 the equation. MATLAB software is used to solve the other program. When substituting into
17 the equation, P needs to adopt a unified international unit system, $P=560000$ Pa. The
18 calculation results and experimental results are shown in Table 5.

19 Table 5. Calculation results of MATLAB

Texture	Calculation results	Experimental results
Chevron texture	0.0856	0.115
Composite texture	0.0913	0.148
Groove texture	0.0887	0.134

1 According to the calculation results, the order of anti-friction performance of different
2 textures from good to bad is as follows: circular, chevron, groove, composite. According to
3 the experimental results, the order of anti-friction performance of different textures from good
4 to bad is as follows: chevron, groove, composite, circular. In terms of friction coefficient,
5 there is a 10%-40% error between the theoretical analysis results and the experimental results.
6 From the simulation analysis, it can be seen that the circular texture is suitable for medium
7 and low speed and high load conditions, and 50 N, 100 r/min are medium speed and low load
8 conditions. The simulation results are consistent with MATLAB calculation results. An
9 important factor that may cause large differences in experimental results may be experimental
10 errors. According to the friction and wear test results of circular texture, the friction
11 coefficient is large under this condition, indicating that there is a greater possibility of errors.
12 Other working conditions were followed the above steps to verify the hydrodynamic
13 lubrication theory. The results prove that the theory has a certain accuracy, but it still has some
14 differences from the actual experimental results, and in-depth research is still needed.

15 **6. Conclusions**

16 In this paper, taking the severe working condition of the friction surface of the key
17 workpiece as the application background, the mathematical model of hydrodynamic
18 lubrication was constructed through theoretical analysis and simulation. The mathematical
19 model was verified through the friction and wear experiment. The purpose is to summarize a
20 set of surface texture theory and optimal selection equations for complex working conditions.

21 It is found that under the same area occupancy rate, texture quantity and experimental
22 conditions, different textures have different tribological characteristics under different

1 working conditions. Circular texture has the strongest pressure-bearing capacity, but the
2 correlation between texture units is weak. The hydrodynamic lubrication effect is not
3 significant at high speeds, and it is suitable for medium and low speed high load conditions.
4 The bearing capacity of chevron texture is second only to circular texture, and the correlation
5 between texture units is better than circular texture, which is suitable for medium and high
6 speed, medium and high load conditions. The pressure capacity of the groove texture is the
7 weakest among the four textures, but the correlation of the texture unit is the best, which is
8 more suitable for high speed and low load working conditions. The composite texture
9 includes the characteristics of circular texture and groove texture. It has certain pressure
10 bearing capacity and good correlation of texture units. It is suitable for high-speed and
11 medium-high load conditions. The mathematical model is verified by the experimental results,
12 and the results show the accuracy and reliability of the theory.

13 **Funding:**

14 The National Natural Science Foundation of China (51575234, 51872122) and the
15 Postdoctoral Science Foundation of China (2017M620286) and The Key Research and
16 Development Program of Shandong Province, China (2018CXGC0809) and Agricultural
17 Machinery Equipment Research and Development Innovation Plan of Shandong Province
18 (2018YF012), Experts from Taishan Scholars and Youth Innovation in Science & Technology
19 Support Plan of Shandong Province University.

20 **References**

- 21 [1] Y.Q. Xing, J.X. Deng, Z. Wu, High friction and low wear properties of laser-textured
22 ceramic surface under dry friction, OPT. LASER. TECHNOL. 93 (2017) 24–32.
- 23 [2] D. Bhaduri, A. Batal, S.S. Dimov, On Design and Tribological Behaviour of Laser
24 Textured Surfaces, Procedia CIRP. 60 (2017) 20–25.

- 1 [3] H.Z. Fan, Y.F. Su, J.J. Song, Design of "double layer" texture to obtain superhydrophobic
2 and high wear-resistant PTFE coatings on the surface of Al₂O₃/Ni layered ceramics,
3 TRIBOL. INT. 136 (2019) 455–461.
- 4 [4] Y.K. Zhou, H. Zhu, W. Tang, Development of the theoretical model for the optimal
5 design of surface texturing on cylinder liner, TRIBOL. INT. 52 (2012) 1–6.
- 6 [5] Z. Zhao, W.Z. Lu, Y.F. He, Research on optimal laser texture parameters about
7 antifriction characteristics of cemented carbide surface, INT. J. REFRACT. MET. H. 82
8 (2019) 287–296.
- 9 [6] G. Ryk, I. Etsion, Testing piston rings with partial laser surface texturing for friction
10 reduction, WEAR. 261 (2006) 792–796.
- 11 [7] I. Etsion, Y. Kligerman, G. Halperin, Analytical and experimental investigation of
12 laser-textured mechanical seal faces, A S L E Transactions. 42 (1999) 511–516.
- 13 [8] M. Wakuda, Y. Yamauchi, S. Kanzaki, Effect of surface texturing on friction reduction
14 between ceramic and steel materials under lubricated sliding contact, WEAR. 254 (2003)
15 356–363.
- 16 [9] K. TONDER, Hydrodynamic effects of tailored inlet roughnesses: Extended theory,
17 TRIBOL. INT. 37 (2004) 137-142.
- 18 [10] M. Fowell, A.V. Olver, A.D. Gosman, Entrainment and inlet suction: Two mechanisms of
19 hydrodynamic lubrication in textured bearings, J. TRIBOL-T. ASME. 129 (2007)
20 336–347.
- 21 [11] A. Hoppermann, M. Kordt, Tribological optimization using laser structured contact
22 surfaces, O+P Oethdraulik and Pneumatik. 46 (2002) 385–392.
- 23 [12] I. Křupka, M. Vrbka, M. Vaverka, Effect of surface dents on contact pressure in
24 elastohydro dynamic contacts, P. I. MECH ENG J-J. ENG. 223 (2009) 683–693.
- 25 [13] I. Křupka, M. Vrbka, M. Hartl, Effect of surface texturing on mixed lubricated
26 nonconformal contacts, TRIBOL. INT. 41 (2008) 1063–1073.

- 1 [14]R. Rahmani, I. Mirzaee, A. Sshirvani, An analytical approach for analysis and
2 optimization of slider bearings with infinite width, *TRIBOL. INT.* 43 (2010) 1551–1565.
- 3 [15]A.G. Charitopoulos, E.E. Efstathiou, C.I. Papadopoulos, Effects of manufacturing errors
4 on tribological characteristics of 3D textured micro-thrust bearings, *CIRP. J. MANUF.*
5 *SCI. TEC.* 6 (2013) 128–142.
- 6 [16]P. Andersson, J. Koskinen, S. Varjus, Microlubrication effect by laser-textured steel
7 surfaces, *WEAR.* 262 (2007) 369–379.
- 8 [17]Y. Kligerman, I. Etsion, Analysis of the hydrodynamic effects in a surface textured
9 circumferential gas seal, *TRIBOL. T.* 44 (2001) 472–478.
- 10 [18]A.Y. Suh, S.C. Lee, A. Polycarpou, Adhesion and friction evaluation of textured slider
11 surfaces in ultra-low head–disk interface, *TRIBOL. LETT.* 17 (2004) 739–749.
- 12 [19]R.T. Tong, B. Han, Z.F. Quan, Molecular dynamics simulation of friction and heat
13 properties of Nano–texture GOLD film in space environment, *SURF. COAT .TECH.* 358
14 (2019) 775–784.
- 15 [20]Z.Y. Li, W.J. Yang, Y.P. Wu, Role of humidity in reducing the friction of graphene layers
16 on textured surfaces, *APPL. SURF. SCI.* 403 (2017) 362–370.
- 17 [21]X.Q. Hao, W. Cui, L. Li, Cutting performance of textured polycrystalline diamond tools
18 with composite lyophilic/lyophobic wettabilities, *J. MATER. PROCESS. TECH.* 260
19 (2018) 1–8.
- 20 [22]S.C. Vlădescu, S. Medina, A.V. Olver, Lubricant film thickness and friction force
21 measurements in a laser surface textured reciprocating line contact simulating the piston
22 ring - liner pairing, *TRIBOL. INT.* 98 (2016) 317–329.
- 23 [23]D.S. Xiong, Y.K. Qin, J.L. Li, Tribological properties of PTFE/laser surface textured
24 stainless steel under starved oil lubrication, *TRIBOL. INT.* 82 (2015) 305–310.
- 25 [24]A. Gherca, A. Fatu, M. Hajjam, Influence of surface texturing on the hydrodynamic
26 performance of a thrust bearing operating in steady–state and transient lubrication regime,

- 1 TRIBOL. INT. 102 (2016) 305–318.
- 2 [25] S. Wos, W. Koszela, P. Pawlus, Determination of oil demand for textured surfaces under
3 conformal contact conditions, TRIBOL. INT. 93 (2016) 602–613.
- 4 [26] Z.R. Zhang, X.W. Zhang, J.H. Yan, Manifold method coupled velocity and pressure for
5 Navier–Stokes equations and direct numerical solution of unsteady incompressible
6 viscous flow, COMPUT. FLUIDS. 39 (2010) 1353–1365.
- 7 [27] L.V. Mirantsev, A.K. Abramyan, Couette flows between various bounding substrates,
8 PHYS. LETT. A. 384 (2020) 126181.

Figures

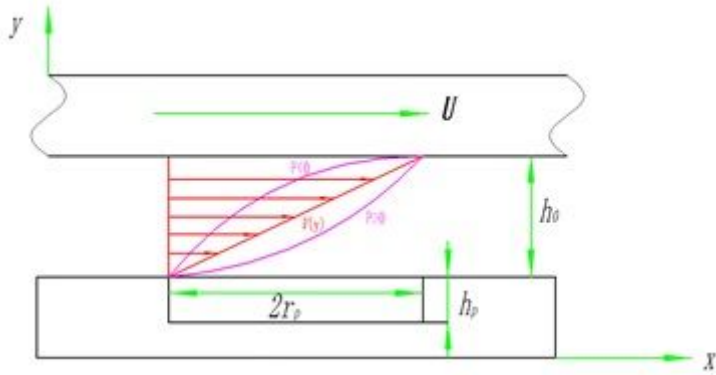


Figure 1

Couette flow

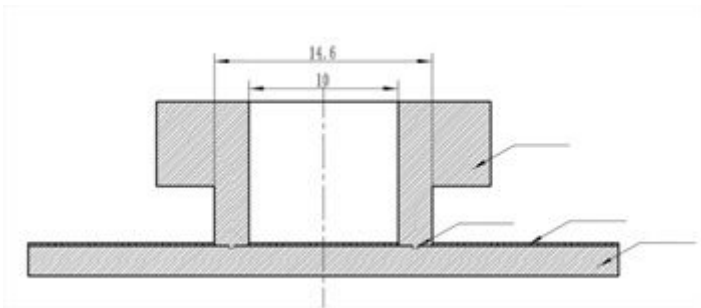


Figure 2

Couette flow

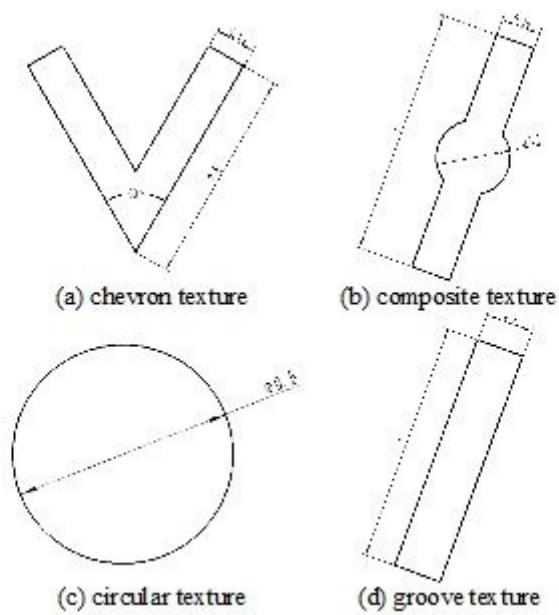
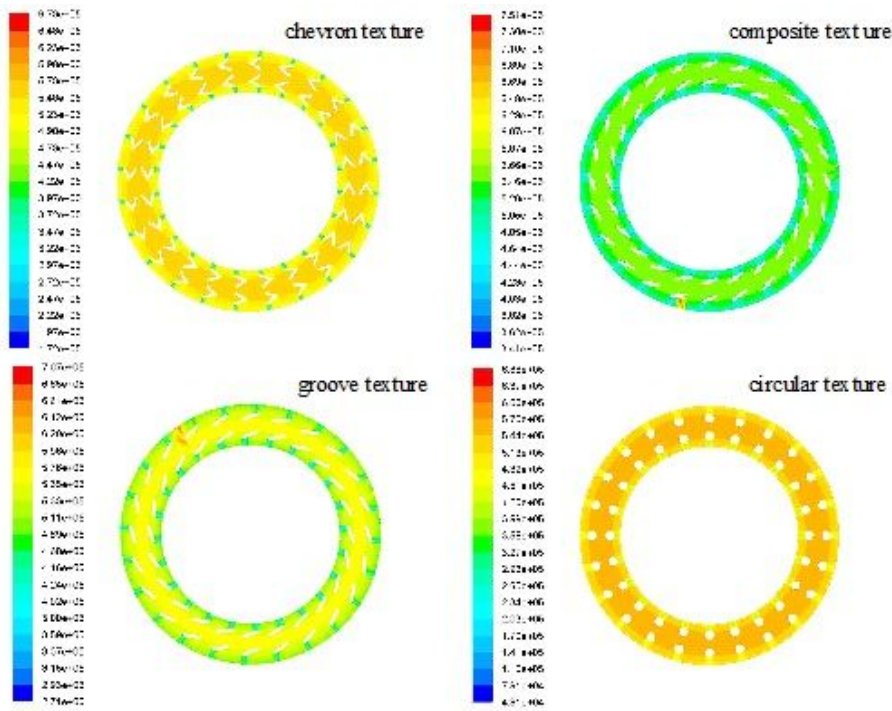
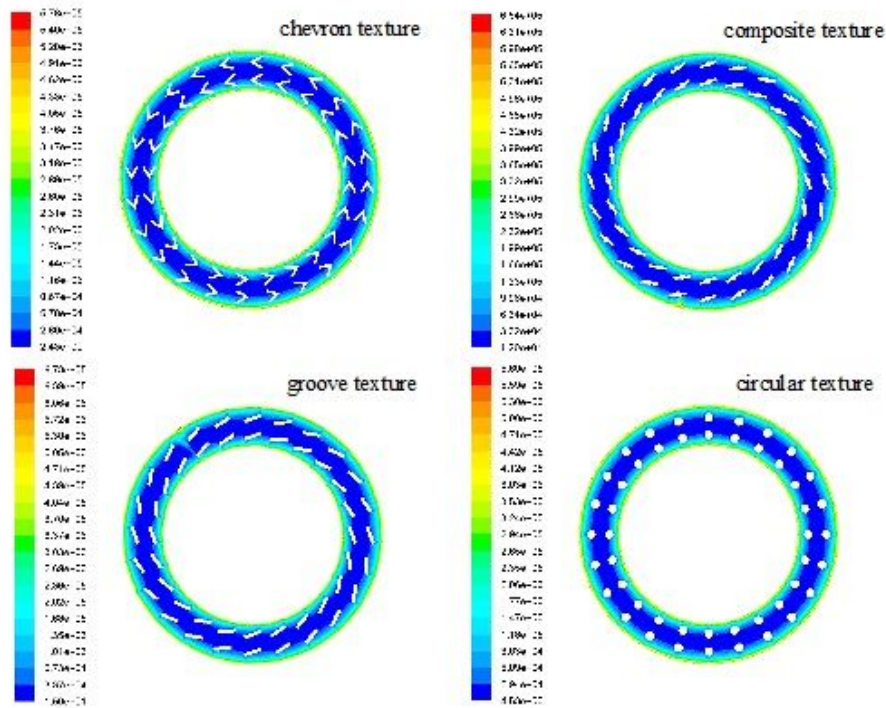


Figure 3

The size of the texture



(a) Overall pressure cloud diagram



(b) Dynamic pressure cloud diagram

Figure 4

Overall pressure cloud diagram and dynamic pressure cloud diagram of overall texture

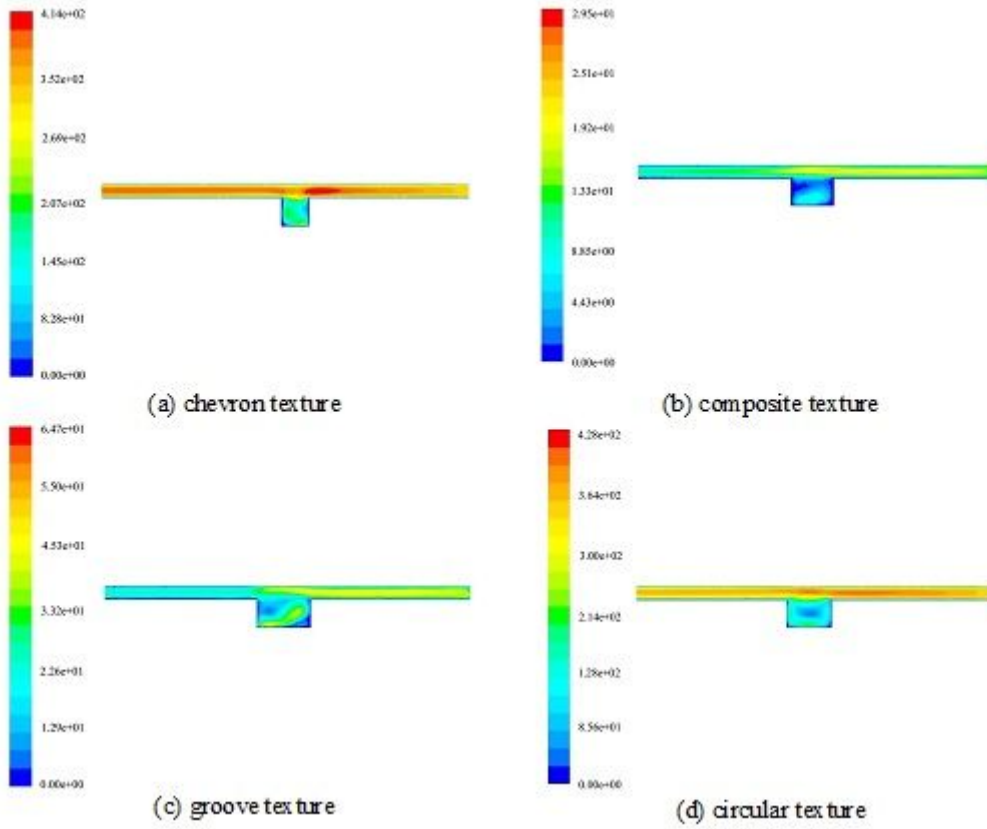


Figure 5

Cloud diagram of velocity distribution

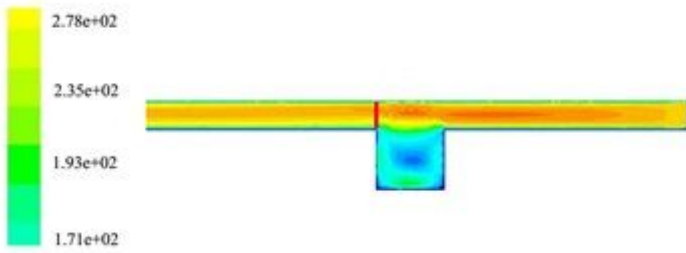


Figure 6

Schematic diagram of the location of the data selection line

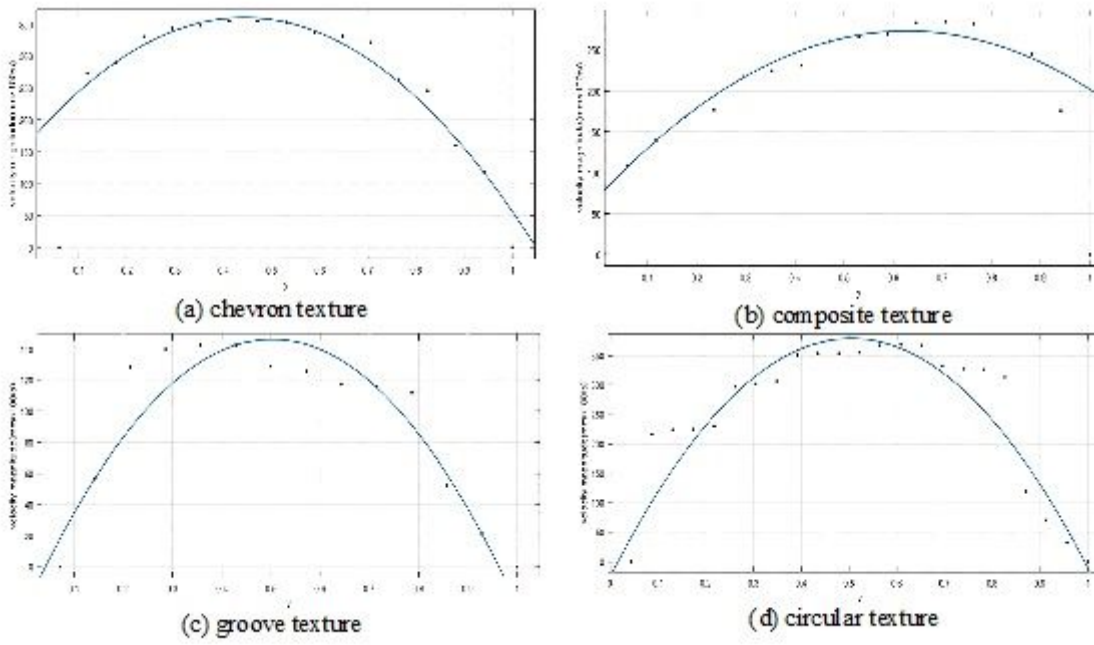


Figure 7

Fitting curves of four textures



Figure 8

Friction and wear testing machine, 45 steel, and workpiece after processing texture

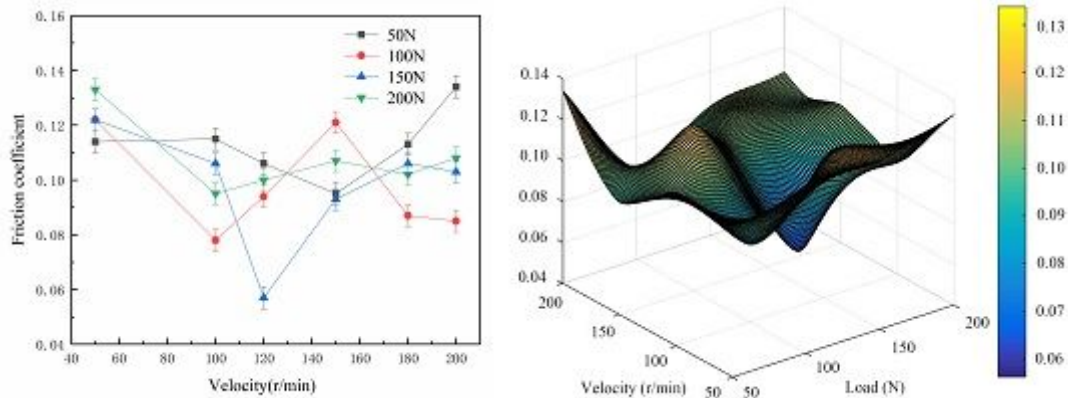


Figure 9

Experimental results of chevron texture

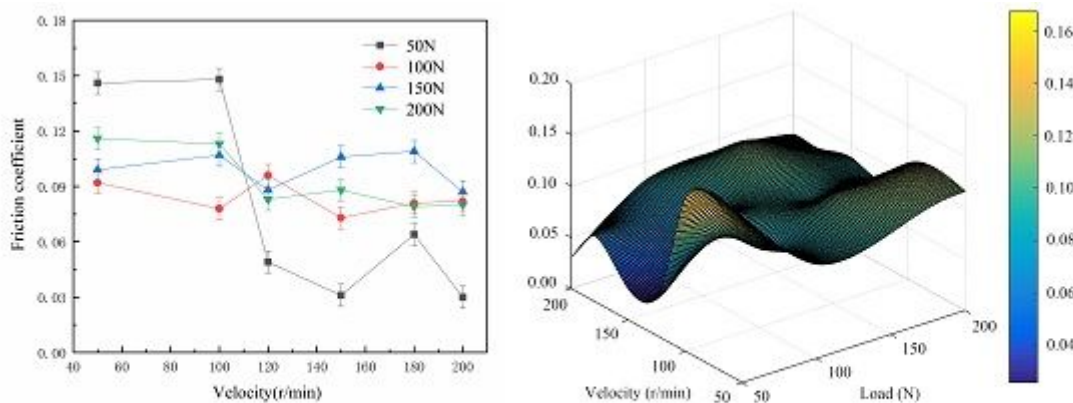


Figure 10

Experimental results of composite texture

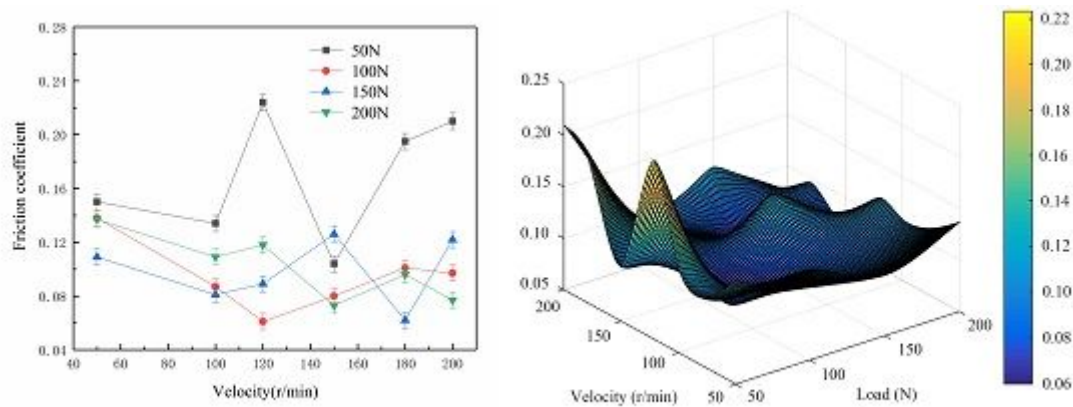


Figure 11

Experimental results of groove texture

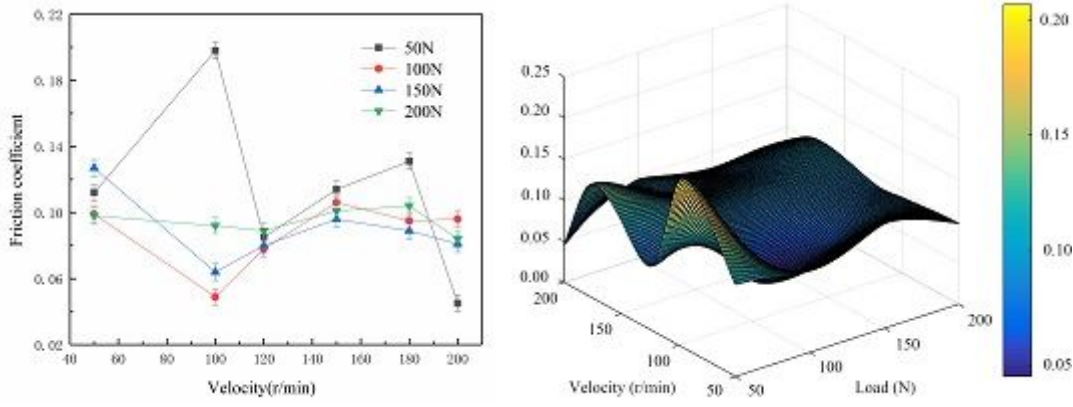


Figure 12

Experimental results of circular texture

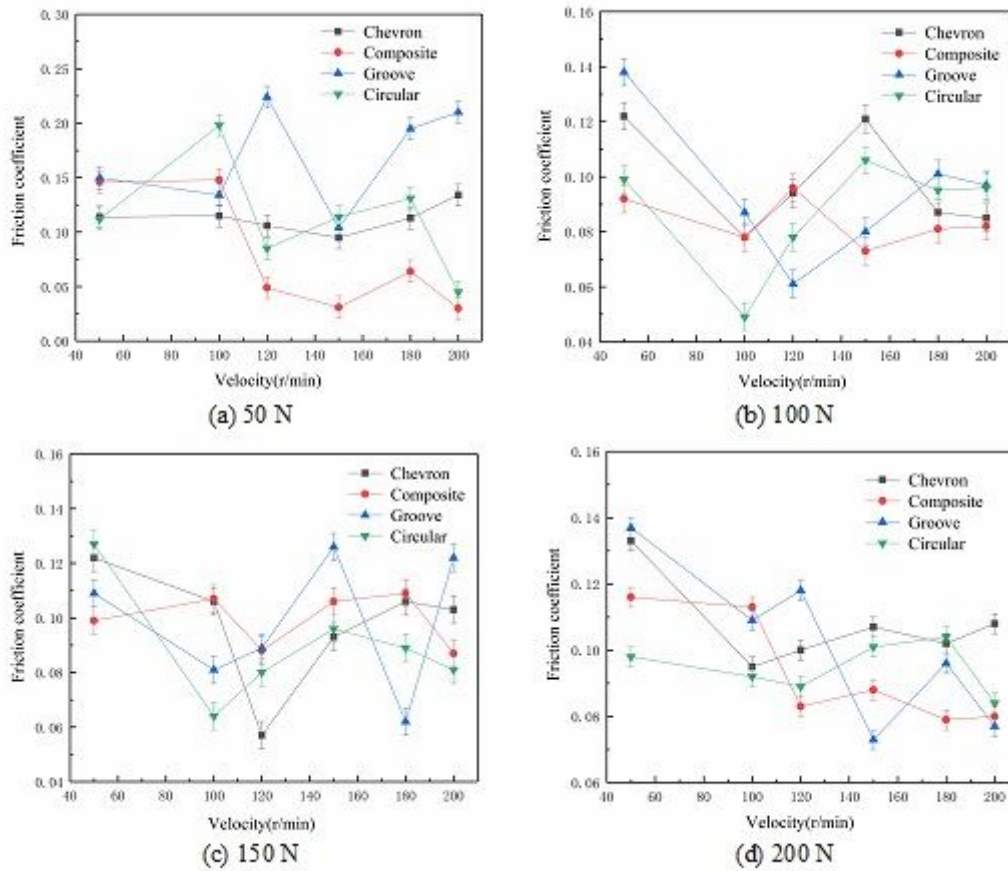


Figure 13

Variation curve of friction coefficient of different textures under the same loading force